LETTERS

Structural signature of jamming in granular media

Eric I. Corwin[1], Heinrich M. Jaeger[1] & Sidney R. Nagel[1]

Glasses are rigid, but flow when the temperature is increased. Similarly, granular materials are rigid, but become unjammed and flow if sufficient shear stress is applied. The rigid and flowing phases are strikingly different, yet measurements reveal that the structures of glass and liquid are virtually indistinguishable[1,2]. It is therefore natural to ask whether there is a structural signature of the jammed granular state that distinguishes it from its flowing counterpart. Here we find evidence for such a signature, by measuring the contact-force distribution between particles during shearing. Because the forces are sensitive to minute variations in particle position, the distribution of forces can serve as a microscope with which to observe correlations in the positions of nearest neighbours. We find a qualitative change in the force distribution at the onset of jamming. If, as has been proposed[3–9], the jamming and glass transitions are related, our observation of a structural signature associated with jamming hints at the existence of a similar structural difference at the glass transition— presumably too subtle for conventional scattering techniques to uncover. Our measurements also provide a determination of a granular temperature that is the counterpart in granular systems to the glass-transition temperature in liquids.

Experiments on granular material provide a unique opportunity to measure quantities that are experimentally inaccessible in more microscopic systems. One such quantity is $P(F)$, the probability distribution of interparticle normal-force magnitudes[10]. For static, jammed granular systems, the shape of $P(F)$ has been studied by experiments and simulations[8,10–21]. For frictional systems, $P(F)$ decays exponentially above the average force, $\langle F \rangle$, and has a plateau or small peak at force magnitudes below $\langle F \rangle$. This characteristic shape of $P(F)$ has become a signature of a jammed granular system[19].

When the applied shear stress is raised above yield, granular material will flow[22]. Above yield, some simulations[19] find the disappearance at high strain rates of the low-force peak in $P(F)$, and others[21] suggest that even below yield $P(F)$ loses its peak parallel to the strain direction. However, another set of simulations finds a negligible change in $P(F)$ on crossing the jamming threshold[23]. The measured distribution of impulses has shown[24] an increase in the number of low impulses at higher flow rates. Hard-sphere simulations[25] interpret this as due to an increase in the probability of high forces. These discrepancies demonstrate the current lack of consensus about any characteristic change in $P(F)$ as the system unjams.

Measurements of $P(F)$ in sheared packings require rapid-response transducers that measure forces on single beads *in situ*. We achieve these requirements by measuring $P(F)$ with a photoelastic plate at the bottom surface of a three-dimensional, cylindrical pack. This plate rotates the polarization of light in proportion to the applied local particle pressure. The position and magnitude of the local pressure is detected by a video camera that views the transducer through an analyser oriented to block any unrotated light (Fig. 1). A roughened piston applying a fixed normal load to the top surface is rotated at a constant rate so that the particle pressures on the bottom surface vary

with time. Extensive calibrations were performed to convert brightness and area values at each contact point into force magnitudes. This method is sensitive to the normal component of force, F, on each bead at the bottom surface of the pack[13,16]. Earlier studies[26,27] showed that measurements of the normal-force distribution at the surface of a pack match those measured within the bulk.

We can also measure the velocity profile of the flow along the bottom plate by tracking the position (without reference to brightness) of the spot that individual particles make on the plate as a function of time. The fixed external wall introduces strong radial shear at the container boundary, and the top surface applies a vertical shear-strain rate that increases linearly with distance, s, from the central axis. The insets to Fig. 2 show the in-plane radial shear-strain rate $\dot{\gamma} = s \, d\omega(s)/ds$ at the bottom surface as a function of radius, s, where $\omega(s)$ is the average angular velocity. For all heights and rotation rates, the radial strain rate is only significant near the outer edge and approaches zero near the central axis where the pack rotates rigidly. It is well fitted by an exponential decay $\dot{\gamma} \propto \exp[-(R_0 - s)/\lambda]$ with characteristic decay length $\lambda \approx 3$–4 bead diameters, where R_0 is the radius of the container.

Data were collected at the bottom surface in a region encompassing approximately 300 beads (bead diameter $d = 3.06 \pm 0.04$ mm), which stretched from the central axis to the outer edge of the pack at the container wall. A typical, hour-long data run provided $\sim 10^4$ frames for analysis, resulting in 3×10^6 distinct force measurements. This allowed determination of the time-averaged distribution, $P(f)$, over small regions of the bottom surface, where the variable f is the force magnitude, F, normalized by its average value across the plate, $\langle F \rangle$. Because the system is cylindrically symmetric, the shearing conditions are uniform in concentric rings around the axis. Thus, a normalized probability distribution of forces, $P_s(f)$, was calculated for each annulus as a function of radius, s (Fig. 2). In this way, we measure $P_s(f)$ within the shear band near the cell boundary as well as in the static region near the axis.

Figures 2a and b show $P_s(f)$ as a function of radius s for 10- and 20-particle-tall packs, respectively. We see a change in shape between the rigid regions near the axis and the sheared regions near the wall. We now show that there is an abrupt transition in $P(f)$ as the shear stress is increased above yield and that $P_s(f)$ from all sheared regions can be collapsed onto a single master curve. Figure 3a demonstrates this collapse for data from all heights, shear rates and applied loads measured.

Our data near the central axis match those of previous measurements taken for static systems of the same height[13,16], which at large forces show a slower than exponential distribution for short packs ($h < 20$) and a simple exponential distribution for taller packs ($h \geq 20$). We have also measured $P_s(f)$ under applied shear stress below yield and find that both the low-force behaviour (Fig. 3b) and the high-force behaviour (Fig. 3c) show no detectable change in the shape of the distribution as long as yield is not exceeded. However, at the outer edge of the pack, within the shear band, $P_{s>12d}(f)$ exhibits markedly different behaviour. First, it shows an enhancement for

[1]James Franck Institute, Department of Physics, The University of Chicago, Chicago, Illinois 60637, USA.

forces smaller than the mean as compared to the static distribution (Fig. 3b). Second, it decays much more rapidly than an exponential.

The change in shape of the high-force part of $P_s(f)$ between the static and flowing regions can be quantified by measuring the curvature for a distribution of the general type $P_s(f) \approx \exp[-f^n]$. To extract the power n, we plot $P_s(f)$ on a (loglog)–(log) graph in the range $P_s(f) < 1$. In this plot, distributions representing the jammed phase would exhibit slope magnitudes no larger than unity ($n = 1$ for strictly exponential shapes and $n < 1$ for the shapes seen at small h). This is confirmed in Fig. 3c which includes data for all heights and shear stresses less than yield. In contrast, as shown in Fig. 3d, our data from the unjammed regime at all heights have slopes n significantly greater than unity.

The shear obtained from the velocity profiles (insets to Fig. 2) is in the radial direction. However, from the geometry of our system, we know that shear in the axial direction must exist as well. Since observed changes in $P_s(f)$ occur only near the container edge and not near its axis, we conclude that $P_s(f)$ is sensitive primarily to a shear band at the measurement surface oriented normal to the direction of force measurement. Little or no change is observed due to the vertical, or axial, shear above the measurement surface oriented parallel to the direction of force measurement.

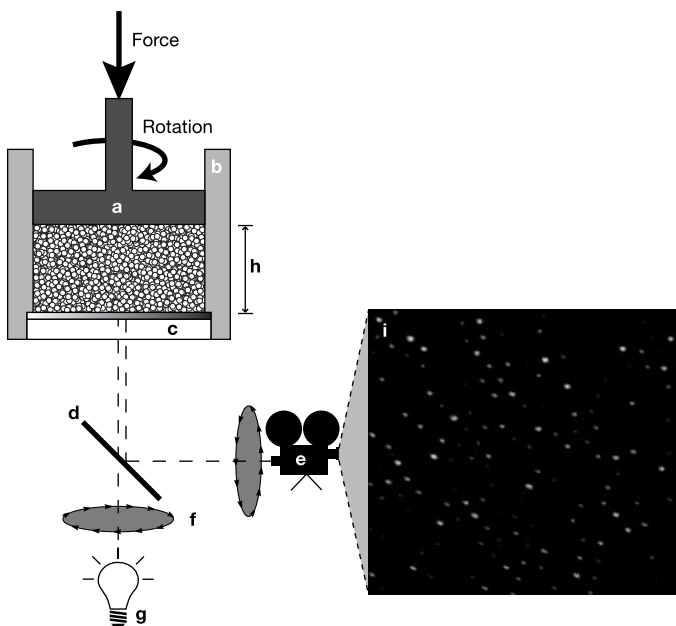To understand $P(f)$ in the flowing regime we start with the analytic calculation of ref. 19, which predicts what $P(f)$ should be in an equilibrium system of interacting particles. Assuming that interparticle normal forces depend only on particle separation, we have $P(f)\mathrm{d}f = G(r)\mathrm{d}r$ where $G(r)$ is the probability of finding particles separated by a distance between r and $r + \mathrm{d}r$. In three dimensions, at asymptotically small r, $G(r) \propto r^2 \exp[-\beta V(r)]$, where $\beta = 1/(k_B T)$, T is the temperature, k_B is Boltzmann's constant, and $V(r)$ is the interparticle potential. Elastic spheres interact with the
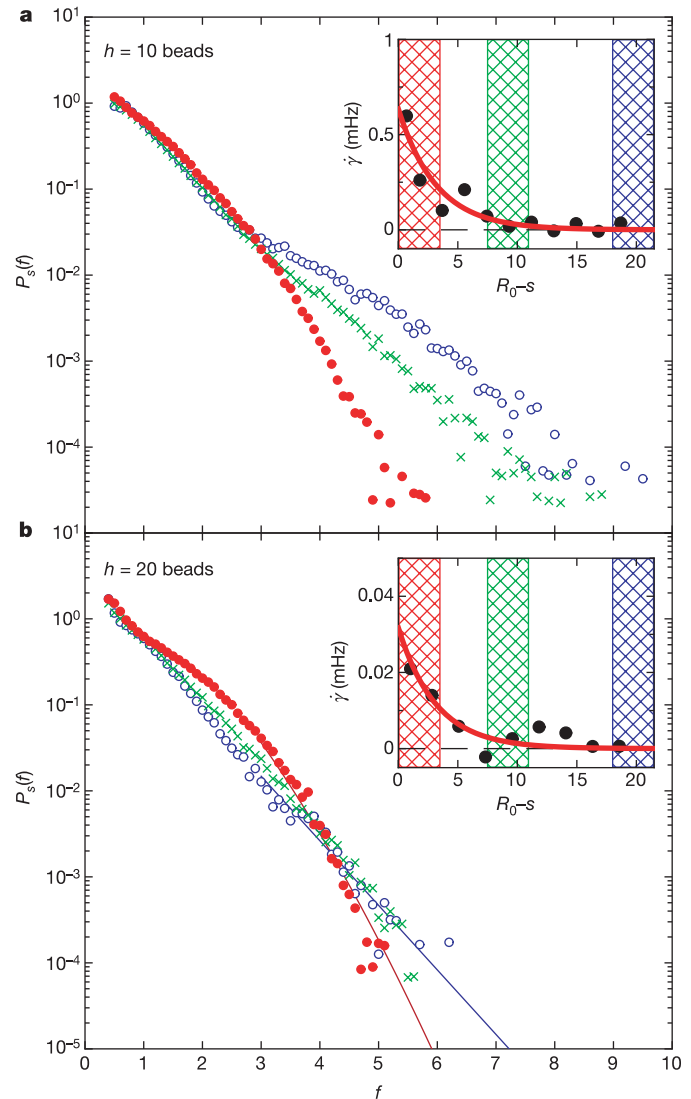
Figure 2 | Change of force probability distributions with local shear strain rate. Main panels, azimuthally averaged distributions, $P_s(f)$, evaluated inside annuli a distance, s, from the rotation centre are plotted for systems of two different filling heights, h. In both panels, data from three annuli are shown: $0 < s < 3.5$ (blue open circles), $10.5 < s < 14$ (green crosses), and $18.5 < s < 21$ (red filled circles). In the non-sheared regions near the centre, $P(f)$ exhibits the same shape as for a static pack (slower than exponential for $h = 10$ and nearly exponential for $h = 20$). In the shearing regions, $P(f)$ acquires the shape of an equilibrium distribution given by equation (1). Guides to the eye in the $h = 20$ graph are drawn to distinguish the data from the inner and outer annuli. Insets, in-plane shear strain rate $\dot{\gamma} = s\mathrm{d}\omega(s)/\mathrm{d}s$ as a function of distance $(R_0 - s)$ from the container wall. The cross-hatched areas indicate the corresponding annular regions in the main panels. Packs rotating as rigid bodies correspond to $\dot{\gamma} = 0$ (dashed line). The decay of the shear strain rate away from the outer wall and towards the centre is well fitted by an exponential with characteristic length $\lambda = 3.2$ bead diameters for both $h = 10$ and $h = 20$ (solid lines). This behaviour is seen at all heights and all shear strain rates studied.

Figure 1 | Experimental set-up. Diagram of shear cell and force measurement apparatus. The bead pack has radius $R_0 \approx 21.5$ beads and heights (h) ranging from 6 to 20 beads, and is composed of soda-lime glass beads 3.06 ± 0.04 mm in diameter. Normal and shear stresses are applied to the bead pack through a roughened piston (**a**) with beads glued to it. For all measurements, a load of 1,380 N was applied by compressing a stiff spring to achieve a nearly constant loading condition. Shear force is applied by a 1/2-h.p. motor (torque 1,112 lb in) driving a 7:1 reduction sprocket to achieve rotation rates from 0.1 to 15 r.p.m. at the top of the bead pack. The bead pack is held in place by a confining cylinder (**b**) with smooth walls. The force transducer (**c**) sits underneath the bead pack, and consists of a 0.25-mm sheet of photoelastic polymer (PS-1E Vishay Measurements Group, Inc., Raleigh, NC) silvered on the top surface and bonded on the bottom to a 3/8-inch-thick clear glass plate. Beads pressing onto the top of the sheet create a local strain field, which rotates incident circularly polarized light. Illumination is provided by a 500-W slide projector (**g**) through a circular polarizer (**f**) and a half-silvered mirror (**d**). The force transducer is imaged by a digital video camera (Sony DCR VX-2000) (**e**) looking through an oppositely polarized circular polarizer (**f**). A sample image of forces taken with this apparatus is shown (**i**).

hertzian potential $V(r) \propto \Delta^{5/2}$, where $\Delta \equiv d - r$ and d is the particle diameter. In equilibrium we predict that for large forces

$$P(f) = \alpha \left[1 + f^{2/3} \frac{\langle \Delta \rangle}{d} \right]^2 \frac{1}{f^{1/3}} \exp\left[-\frac{\beta}{\beta_0} f^{5/3} \right] \qquad (1)$$

where $\langle \Delta \rangle$ is the average deformation of a bead, $1/\beta_0$ is a temperature scale set by the average force per bead and the bead elastic modulus, and α is a normalization constant. Typical values of $\langle \Delta \rangle / d$ are about

3×10^{-5} so the first term in brackets can, to high accuracy, be replaced by unity. For very small forces, we can expand $G(r)$ around $r = d$. As long as there is any pressure in the system, G is a constant to leading order so we again obtain the low-force behaviour: $P(f) \propto f^{-1/3}$.

This model predicts that all data in the shear band at both high and low forces will follow a master curve if plotted as $P_s(f) T_{\text{eff}}^{1/5} / \alpha$ versus $f/T_{\text{eff}}^{3/5}$, where $T_{\text{eff}} \equiv \beta_0/\beta$ is a dimensionless effective temperature.
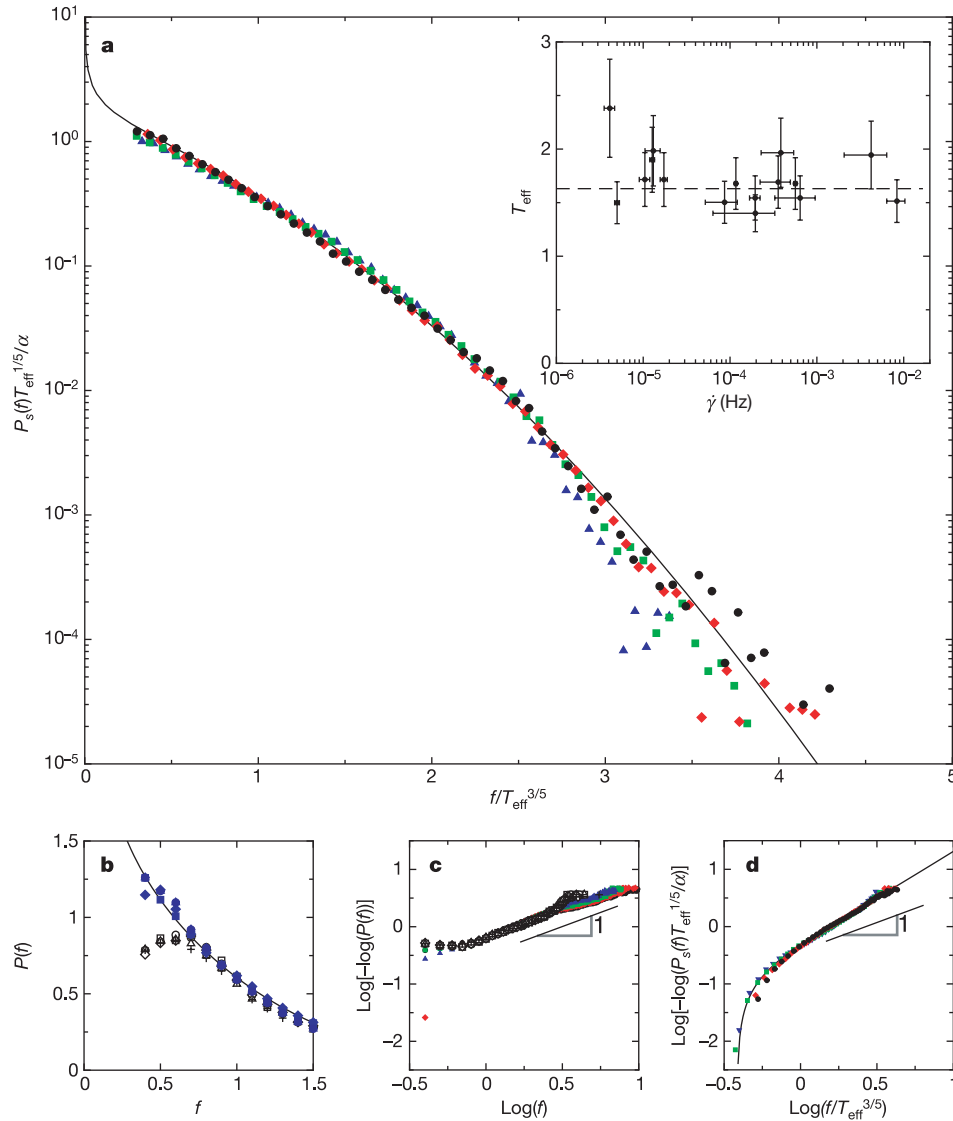

Figure 3 | Comparison between force probability distribution and equilibrium hertzian model. a, Scaled distributions $P_s(f) T_{\text{eff}}^{1/5} / \alpha$ in the sheared region as a function of scaled force magnitude $f/T_{\text{eff}}^{3/5}$. Data from shearing regions (outer annulus, $18.5 < s < 21$) collapse onto a single master curve for all heights: $h = 6$ (black circles), 10 (red diamonds), 15 (green squares) and 20 (blue triangles). The solid line is the prediction of the hertzian model, equation (1). Inset, effective temperature, T_{eff}, obtained from the data collapse for packs of all heights, as a function of shear strain rate, $\dot{\gamma}$. The error bars in T_{eff} are associated with fitting our model to $P_s(f)$. The error bars in $\dot{\gamma}$ are the standard deviation of particle shear strain rates measured across the shearing annulus. Within experimental accuracy, there is no evolution of effective temperature with shear-strain rate over 3.5 orders of magnitude, from $\dot{\gamma} = 5 \times 10^{-6}$ Hz to 10^{-2} Hz. The dotted line shows the average value $\langle T_{\text{eff}} \rangle = 1.63$. The difference between the static and the sheared behaviour as well as the close agreement between sheared behaviour and the hertzian model is shown in greater detail for low forces in the linear–linear plot (**b**) and for asymptotically high forces in the loglog–log plots (**c** and **d**).

b, Enhancement of $P_s(f)$ at low forces in the shearing region as compared to a static material. Solid blue symbols are data from **a** (circles $h = 6$, diamonds $h = 10$, squares $h = 15$, triangles $h = 20$). This is contrasted with measurements from static packs (all with $h = 20$) at zero shear stress (open black squares), 1/4 yield stress (open black circles), 1/2 yield stress (open black diamonds), 3/4 yield stress (open black triangles), and just below yield (black crosses). The solid line shows the fit given by the hertzian contact model. **c,** Plot of $\log[-\log(P_s(f))]$ versus $\log(f)$ in the high-force regime $P_s(f) < 1$ for the inner, static region of sheared packs ($h = 6$ (black circles), 10 (red diamonds), 15 (green squares) and 20 (blue triangles)) and static packs ($h = 20$) experiencing shear stresses between zero up to just below yield (same symbols as **b**). **d,** Plot of $\log[-\log(P_s(f) T_{\text{eff}}^{1/5}/\alpha)]$ versus $\log(f/T_{\text{eff}}^{3/5})$ in the high-force regime $P_s(f) < 1$ for the outer, shearing region (same data as in **a**). The solid line shows the fit given by the full hertzian contact model, equation (1), which has an asymptotic slope of $+5/3$. A slope of $+1$ corresponding to an exponential $P_s(f)$ is drawn for comparison in **c** and **d**.

Figure 3a demonstrates that data from multiple heights do indeed collapse onto a single curve in excellent agreement with equation (1). In the shearing region the flowing material thus behaves as if it were in equilibrium at temperature T_{eff}. This T_{eff} reflects the ability to explore phase space under shear.

We find that T_{eff} in the shearing region of our pack is insensitive to the measured shear rate at the bottom surface over a range from $\dot{\gamma} = 5 \times 10^{-6}$ to 10^{-2} Hz (Fig. 3 inset). The effective temperature is insensitive to pack height from $h = 6$ to 20 beads as well as to the driving angular velocity of the top plate. This flat behaviour of T_{eff} as a function of $\dot{\gamma}$ is similar to that seen in simulations by Ono et al.[28] of sheared systems where, at asymptotically slow strain rates, the effective temperature was interpreted as the temperature where the amorphous glass becomes a liquid. Ono et al. normalized their temperatures by the amount of energy necessary to move one particle past its neighbour. If we normalize our T_{eff} in the same way we find values between 0.001 and 0.002, consistent with 0.0015 as obtained in the Ono et al. simulations. The stated values are obtained from $T_{eff}/(\beta_0 \mu \langle F \rangle d)$ where μ is the coefficient of friction between glass spheres[16] and β_0 is the energy stored in a bead compressed by a force $\langle F \rangle$ (ref. 29). Even if we allow μ to vary over a full range of reasonable values our effective temperatures will remain of the same order of magnitude.

Our results demonstrate a clear signature of the jamming/unjamming transition which manifests itself in the shape of the distribution of normal forces $P(f)$. Jammed packings are characterized by a distribution that decays exponentially at large forces. As recent simulations have shown, this shape reflects the non-equilibrium character of the jammed state[18]. By contrast, $P(f)$ in the flowing regime is well described by a model that assumes that the system is in equilibrium. Analysis of the shape of $P(f)$ in this regime gives both the functional form of the interparticle potential (in our case the hertzian potential, as appropriate for glass spheres at contact) and an effective granular temperature.

In molecular systems, measurements of structural changes typically focus on the pair correlation function, $g(r)$. A measurement of $P(f)$ has several advantages over measuring the pair correlation function. First, even a small polydispersity broadens $g(r)$ but leaves $P(f)$ unaffected since forces depend on compression from the point of contact rather than absolute interparticle distance. Second, even a tiny change in the interparticle spacing produces an extremely large change in the force. This makes the measurement of forces particularly sensitive to interparticle spatial correlations. The result of this paper on the signature of flowing versus jammed systems observed in $P(f)$ hints that such a signature might also exist at the glass transition. Moreover, the result that a flowing granular material can be approximately understood in terms of an equilibrium theory adds credence to the idea of a jamming phase diagram[3]. Although the region at large shear strain rate is flowing and so not in true equilibrium, it can, nonetheless, be described in terms of equilibrium distributions; that is, the shear rate can be thought of as simply producing an effective temperature which allows the material to explore phase space.

1. Frick, B. & Richter, D. The microscopic basis of the glass-transition in polymers from neutron-scattering studies. *Science* **267**, 1939–1945 (1995).
2. Leheny, R. L. et al. Structural studies of an organic liquid through the glass transition. *J. Chem. Phys.* **105**, 7783–7794 (1996).
3. Liu, A. J. & Nagel, S. R. Nonlinear dynamics—Jamming is not just cool any more. *Nature* **396**, 21–22 (1998).
4. Liu, A. J., Nagel, S. R. (eds) *Jamming and Rheology. Constrained Dynamics on Microscopic and Macroscopic Scales* (Taylor and Francis, London, 2001).
5. Silbert, L. E., Ertas, D., Grest, G. S., Halsey, T. C. & Levine, D. Analogies between granular jamming and the liquid-glass transition. *Phys. Rev. E* **65**, 051307 (2002).
6. Coniglio, A., Fierro, A., Herrmann, H. J. & Nicodemi, M. (eds) *Unifying Concepts in Granular Media and Glasses* (Elsevier, Amsterdam, 2004).
7. Trappe, V., Prasad, V., Cipelletti, L., Segre, P. N. & Weitz, D. A. Jamming phase diagram for attractive particles. *Nature* **411**, 772–775 (2001).
8. Lacevic, N. & Glotzer, S. C. Dynamical heterogeneity and jamming in glass-forming liquids. Preprint at ⟨http://ArXiv.org/cond-mat/0406451⟩ (2004).
9. Howell, D., Behringer, R. P. & Veje, C. Stress fluctuations in a 2D granular Couette experiment: A continuous transition. *Phys. Rev. Lett.* **82**, 5241–5244 (1999).
10. Liu, C. H. et al. Force fluctuations in bead packs. *Science* **269**, 513–515 (1995).
11. Howell, D. & Behringer, R. P. in *Powders and Grains 97* (eds Behringer, R. P. & Jenkins, J. T.) 337–340 (Balkema, Rotterdam, 1997).
12. Baxter, G. W. in *Powders and Grains 97* (eds Behringer, R. P. & Jenkins, J. T.) 345–348 (Balkema, Rotterdam, 1997).
13. Blair, D. L., Mueggenburg, N. W., Marshall, A. H., Jaeger, H. M. & Nagel, S. R. Force distributions in three-dimensional granular assemblies: Effects of packing order and interparticle friction. *Phys. Rev. E* **63**, 041304 (2001).
14. Løvoll, G., Måløy, K. J. & Flekkøy, E. G. Force measurements on static granular materials. *Phys. Rev. E* **60**, 5872–5878 (1999).
15. Makse, H. A., Johnson, D. L. & Schwartz, L. M. Packing of compressible granular materials. *Phys. Rev. Lett.* **84**, 4160–4163 (2000).
16. Mueth, D. M., Jaeger, H. M. & Nagel, S. R. Force distribution in a granular medium. *Phys. Rev. E* **57**, 3164–3169 (1998).
17. Silbert, L. E., Grest, G. S. & Landry, J. W. Statistics of the contact network in frictional and frictionless granular packings. *Phys. Rev. E* **66**, 061303 (2002).
18. O'Hern, C. S., Silbert, L. E., Liu, A. J. & Nagel, S. R. Jamming at zero temperature and zero applied stress: The epitome of disorder. *Phys. Rev. E* **68**, 011306 (2003).
19. O'Hern, C. S., Langer, S. A., Liu, A. J. & Nagel, S. R. Force distributions near jamming and glass transitions. *Phys. Rev. Lett.* **86**, 111–114 (2001).
20. Edwards, S. F. & Grinev, D. V. Statistical mechanics of granular materials: stress propagation and distribution of contact forces. *Granular Matter* **4**, 147–153 (2003).
21. Snoeijer, J. H., Vlugt, T. J. H., van Hecke, M. & van Saarloos, W. Force network ensemble: A new approach to static granular matter. *Phys. Rev. Lett.* **92**, 054302 (2004).
22. Conway, S. L., Shinbrot, T. & Glasser, B. J. A Taylor vortex analogy in granular flows. *Nature* **431**, 433–437 (2004).
23. Landry, J. W., Grest, G. S. & Plimpton, S. J. Forces in granular hopper flow. *Bull. Am. Phys. Soc.* **48**, 153 (2003).
24. Longhi, E., Easwar, N. & Menon, N. Large force fluctuations in a flowing granular medium. *Phys. Rev. Lett.* **89**, 045501 (2002).
25. Ferguson, A., Fisher, B. & Chakraborty, B. Impulse distributions in dense granular flows: Signatures of large-scale spatial structures. *Europhys. Lett.* **66**, 277–283 (2004).
26. Radjai, F., Roux, S. & Moreau, J. J. Contact forces in a granular packing. *Chaos* **9**, 544–550 (1999).
27. Brujic, J., Edwards, S. F., Hopkinson, I. & Makse, H. A. Measuring the distribution of interdroplet forces in a compressed emulsion system. *Physica A* **327**, 201–212 (2003).
28. Ono, I. K. et al. Effective temperatures of a driven system near jamming. *Phys. Rev. Lett.* **89**, 095703 (2002).
29. Landau, L. D. & Lifshitz, E. M. *Theory of Elasticity* Ch. 1, 3rd edn, Sect. 9 (Butterworth-Heinemann, Oxford, 1986).